BODY WING TAIL INTERFERENCE STUDIES AT HIGH ANGLES OF ATTACK AND VARIABLE REYNOLDS NUMBERS

K. Hartmann and V. Kanagarajan [1]
Deutsche Forschungs- und Versuchsanstalt für Luft- und Raumfahrt e.V.
Institut für Experimentelle Strömungsmechanik
D-3400 Göttingen, Bunsenstraße 10, FRG

and

D. Nikolitsch
Messerschmidt Bölkow Blohm GmbH
Unternehmensbereich Apparate
D-8000 München-Ottobrunn, FRG

Abstract

Six component measurements were carried out in two wind tunnels on several combinations of an ogive-circular cylinder body without and with lifting surfaces having rectangular planform area and sharp leading and trailing edges. These experiments were performed in the incompressible and subsonic compressible speed range at various Reynolds numbers up to high angles of attack. For the same geometries the forces and moments were calculated and compared with the experimental results. It was the aim of this combined investigations to get a better understanding of the vortex flows over such body-wing-tail combinations, to verify the applied prediction methods and to obtain hints for a more accurate theoretical modelling of the flow field.

Nomenclature

Alfa, α	Angle of attack
AR	Aspect ratio
c_r	Wing aerodynamic root chord
$Cm = M/(q_\infty \cdot S \cdot D)$	Pitching moment coefficient
$CN = Z/(q_\infty \cdot S)$	Normal force coefficient
$Cn = N/(q_\infty \cdot S \cdot D)$	Yawing moment coefficient
$CY = Y/(q_\infty \cdot S)$	Side force coefficient
	* Orientation of all forces and moments see system of co-ordinates in Fig. 1
D	Body diameter, reference length, 35 mm
h	Thickness of rectangular wing
M	Pitching moment; reference point is body nose tip
N	Yawing moment; reference point is body nose tip
p	Freestream static pressure
p_0	Stagnation pressure
$q_\infty = (1/2)\rho V_\infty^2$	Freestream dynamic pressure
Re	Reynolds number, based on body diameter
$S = (\pi D^2)/4$	Body cross-section, reference area
T, t	Freestream temperature
V_∞	Freestream velocity
XCP	Distance of center of pressure of the normal force behind body nose tip
x, y, z	Cartesian co-ordinates, origin in body nose tip, see Fig. 1
Y	Side force
Z	Normal force
α, Alfa	Angle of attack
$\alpha_{Str.}$	Angle of limiting streamline on the body with respect to body longitudinal axis, see Fig. 16
$(\alpha_{Str.})_{theo}$	Estimated angle of limiting streamline on the body with respect to body longitudinal axis, see Fig. 16
φ	Roll position of the lifting surfaces relative to the body, see Fig. 1
Φ	Body roll angle about longitudinal axis, $\Phi = 0°$ arbitrary, see Fig. 1
$\Phi_{1.Sep}$	Circumference angle of first separation on the body, measured from stagnation line, see Fig. 16
$\Phi_{2.Sep}$	Circumference angle of second separation on the body, measured from stagnation line, see Fig. 16
ρ	Freestream density
η	Freestream dynamic viscosity

I. Introduction

The 3-d flow fields around slender bodies without and with lifting surfaces are very complex and predominantly dependent on the geometry of the combinations, the angle of attack, the Mach and Reynolds number. The complexity of such flows causes great difficulties in the understanding of the underlying flow phenomena and their theoretical treatment. At higher angles of attack the flow separates from the body and lifting surfaces. Consequently, vortices are shed from the configurations in different ways and a variety of flow patterns in the leeside can occur. This flow structure produces large forces and moments in the pitch and yaw plane in a non-linear way.

In this connexion the body alone is the most complicated component of a body-wing-tail combination because the positions of the separation lines are not fixed on it, as in the case of a sharp-edged wing. The flow separates from the body along lines which result from the interaction of the external flow with laminar or turbulent boundary layers. The state of the boundary layer prior to the separation has a striking influence on the aerodynamic loads which therefore depend considerably on the Reynolds number. Regarding the Reynolds number it is a problem to decide which kind of definition (characteristic length)

describes best the transition and separation process of a 3-d boundary layer.

On the other hand the transition from an attached flow to a completely separated flow of a wing is reached already at low angles of attack particular with higher aspect ratios.

A great influence on the experimental results can also have the special test conditions of a wind tunnel given by the flow unsteadiness (turbulence level and structure), the model vibration (no ideally rigid model-support-system) and manufacturing imperfections on the body nose tip, on the wings and on their surfaces. The latter lead, at least in case of the body, to a strong dependence of the forces and moments on the body roll position (Φ) and turbulence as shown by K. Hartmann[1].

In addition to the phenomena just described further problems are caused by the mutual interaction of the vortices arising from the body and the lifting surfaces of a body-wing-tail combination.

Starting from the background mentioned before a detailed test program has been established in order to investigate the complicated vortex flow fields over slender bodies in combination with lifting surfaces at high incidences and at various Reynolds numbers. Table 1 comprises the test conditions. The experimental results are considered as a contribution to the improvement of existing codes. Such computational methods which can provide reliable results at low costs are a useful tool in applied aerodynamics.

II. Models

For a comprehensive research program a modular construction of a model was realized which offers a great variety of combinations. From these the combinations as depicted in Figure 1 were selected for the present investigations. These combinations comprise the body alone (ogive plus circular cylinder), two body-tail combinations of cruciform configuration with 3D or 4D span (D = 35 mm, body diameter), respectively and a body-wing-tail combination with a cruciform wing of 3D span and a cruciform tail of 4D span. The leading edges of the cruciform wing are positioned at a distance of 4D behind the body nose tip. All lifting surfaces are rectangular panels with sharp leading and trailing edges. Their chord length is 1D. The wing and tail panels are mounted on sleeves which are parts of the body. These sleeves can be rotated about the body longitudinal axis and fixed at any roll position (φ) relative to the body. All components of the models are made of steel to very close tolerances and with a high degree of surface finish. For surface flow visualizations the models were darkened first by browning and later by a black painting. Further informations were given by V. Kanagarajan and K. Hartmann[2,3,4].

III. Wind tunnels and test set-up

The measurements were carried out in two wind tunnels. One of them is the high speed wind tunnel (HKG) of the DFVLR/AVA used for the subsonic compressible speed range (Ma = 0.4, 0.6 and 0.8). The other one is the 0.6 m pressurized low speed wind tunnel of the DFVLR/AVA in which the influence of the Reynolds number was investigated.

A sketch of the high speed wind tunnel (HKG) is given in Figure 2. This tunnel is of the suck-down type and works between the atmosphere and a vacuum container with a capacity of 10 000 m³. The present experiments were performed in the open-jet subsonic test section of this tunnel. Figure 3 demonstrates how in this tunnel the Reynolds number changes with the Mach number. The basic model support allows a pitch range of -10° to 30°. A detailed decription of this tunnel was given by H. Ludwieg and Th. Hottner[5,6].

The 0.6 m pressurized low speed wind tunnel is of the closed circuit type and can be run continuously. The velocity in the test section can be varied from 0 to a maximum of 38 m/sec by means of a fan, driven by an AC electric motor. Figure 4 shows a sketch of this tunnel which can be charged with compressed air up to 100 bars. The performance envelope of this tunnel is depicted in Figure 5. With the normal model support of this tunnel angles of attack from -30° to 30° are achievable. H. Försching, E. Melzer and G. Schewe[7] described this tunnel in more detail.

In both wind tunnels cranked pieces were used in combination with the basic sting supports to reach angles of attack up to 65° or somewhat more.

For the force and moment measurements two strain gauge balances (TASK Corporation, USA) of different load ranges and an outer diameter of 0.75″ were used. The more rigid one with the higher load range was utilized in the pressurized wind tunnel. Figure 6 shows the test set-up of the high speed wind tunnel.

The electrical outputs of the balances were acquired by the electronic data acquisition systems of the wind tunnels and processed on the main computer of the DFVLR/AVA.

IV. Test program

The test program for both wind tunnels is compiled in Table 1. At the beginning of the experiments the body alone was rolled over 360° in steps of 60° in order to identify a body roll position which yielded a highly asymmetric flow structure on the leeside. The starting roll position of Φ = 0° is arbitrary and was marked on the body. Great flow asymmetry was found at Φ = 60°. At all tests the body was kept at this Φ = 60° roll orientation. Under this condition the lifting surfaces were added to the body in order to get strong interference effects of the asymmetric body vortices on the wing and tail panels which were mainly intended to investigate. Measurements were made for the + ($\varphi = 0°$) and × ($\varphi = 45°$) position of the wing and tail, see Figure 1.

Out of the test conditions of Table 1 more aerodynamic force and moment data were also taken[2,3,4], but due to space limitation, they will not be presented here.

V. Results

Calculations

The numerical technique used in this report for the computation of the aerodynamic coefficients of cruciform wing-body combinations for high angles of attack

1872

and for arbitrary roll angles in the subsonic speed range is based primarily on a coefficient synthesis of the components body and wing. This method is a very useful, fast and inexpensive tool for the prediction of the aerodynamic characteristics of slender wing-body and body-wing-tail combinations, and facilites the design of such configurations.

Calculations were performed and compared with measurements of this report in order to check the limits of the validity of the method. The configurations applied within this test procedure represent rather challenging geometries with regard to theoretical treatment because of the long body and the relatively high aspect ratio wings. A wide range of angles of attack at subsonic Mach numbers was investigated in order to define areas of possible improvements.

The main problems which are associated with high angles of attack are largely characterized by flow separation which leads to a distinct non-linear relationship between angle of attack and the aerodynamic coefficients. This must be taken into account when modelling the flow field around body-wing-tail combinations. The present approach is particularly described in several reports[8,9,10,11].

The linear part of the body aerodynamics is treated with slender body theory or optionally with a 3-d method of source distributions on the body surface. The non-linear part of the body aerodynamics was simulated by a multi-vortex model. This flow model works with asymmetric vortex arrangements, so that 'out of plane' forces and moments can be estimated. The vortex shedding is controlled by Strouhal number. The vortex trajectories are evaluated numerically. The forces and moments of a cruciform wing are calculated by a non-linear lattice method as described by D. Nikolitsch[9]. It was assumed that the free vortex sheets leave the cruciform wing inclined by a half of the local angle of attack. The influences of the body and the velocity field induced by the body vortices were taken into account by computing the downwash on the cruciform wings. Incidentally this approach is similar to the method of 'equivalent angle of attack'. Whereas the influence of the wing on the body is covered by the interference factor $K_B(w)$ according to Nielsen[12], the Mach number effects are taken into account by the Prandtl-Glanert factor.

Tests have shown that this numerical technique leads to sufficiently accurate results at higher angles of attack if the aspect ratio of the wing is small enough. This can be observed here too: The configuration with the wing of 3D span (Fig. 9a,b) agrees better with experiments than the configuration with the wing of 4D span (Fig. 10a,b). This is evident when the moment curves are considered. At higher angles of attack the aerodynamic coefficients are in general overestimated. A possible explanation of this effect is that the lift and moment breaks down at the wing. The local angle of attack at the wing is larger than the angle of attack of the combination (see for instance Fig. 16), so the critical angle of attack (α_{crit}, definition see Fig. 17a,b) is reached sooner. Figure 17a,b shows a typical behaviour of the normal force and moment curves measured by Esch[13]. Using an empirical wing data base for $\alpha > \alpha_{crit}$ instead of the theoretical calculation in this range the coefficient synthesis

shows very good agreement with experiment up to high angles of attack. This is demonstrated in Figure 8a,b. All other examples in this report are calculated without this correction. It is therefore believed that an improvement of this approach can be achieved by developing a method which is able to describe the separated flow over wings within the frame of the component synthesis technique.

Experiments

For the four model combinations described in section II the data of the normal forces, pitching moments, side forces and yawing moments are given in this paper in form of their coefficients. All data are plotted in Figures 7 to 15 and connected by thin lines. As far as available the calculated results are also depicted in Figures 7 to 13. They are represented by thick lines. All values of the Mach and Reynolds numbers in the legends of Figures 7 to 15 are averages with a tolerance of less than 1% for the Mach number and less than 2% for the Reynolds number.

Body alone

The measured forces and moments show a strong non-linear characteristic with the angle of attack. In addition they are dependent on both Mach number and Reynolds number. Note that in the subsonic compressible speed range (Ma = 0.4, 0.6 and 0.8) the Reynolds number changes somewhat with the Mach number because this is conditioned by the wind tunnel. As long as the cross-flow Mach number is small in comparison with its critical value the influence of the Reynolds number predominates. It was shown in other investigations[14,15,16] that at small angles of attack and at Reynolds numbers as in Figure 7 a turbulent separation takes place resulting in small values of the normal forces. With increasing angle of attack the influence of the body vortices becomes stronger and the separation passes into its critical mode (critical Reynolds number regime) accompanied by increasing normal forces. At Mach numbers greater than 0.4 the critical cross-flow Mach number is reached in the present case at $\alpha \approx 45°$ or 32°, respectively. This introduces additional effects, i.e. shock boundary layer interactions. Higher values of the normal forces were obtained at higher Mach numbers. The increase of the aerodynamic coefficients caused by the Mach number at high incidences is greater than at moderate angles of attack where the change is mainly caused by the Reynolds number.

The flow field around the body becomes asymmetric approximately at $\alpha \approx 10°$ which leads to the onset of side forces as can be seen in Figure 7c. With increasing angle of attack the side forces grow, change its directions and reach maximum values within the range of about 40° to 50° and decrease after that at higher incidences. In the subsonic compressible speed range the side forces are about 50% and less smaller than the normal forces. They become smaller with growing Mach number.

The remarkable Reynolds number dependence of the normal and side forces in the incompressible speed range (Ma < 0.1) is demonstrated in Figure 14. These data were obtained in the 0.6 m pressurized low speed wind tunnel. At the highest Reynolds numbers and angles of attack between

about 45° and 65° the body has got into catastrophic vibrations. When this happened the tunnel had to be stopped immediately in order to avoid the damage of the balance. Thus the measurements in this incidence range were not possible. Therefore, there is a lack of data points in Figures 14 and 15.

Up to angles of attack of about 40° the effective Reynolds numbers (Re/sinα) are so high that the flow separates turbulent leading almost to the same normal forces at all Reynolds numbers of these experiments. This corresponds to the transcritical Reynolds number regime of the 2-d circular cylinder with constant drag values. At higher angles of attack, starting at $\alpha \approx 40°$, the 3-d structure of the leeside flow field passes into the 2-d nature growing upstream from the body base. Therefore, the normal forces of the present body at $\alpha = 90°$ correspond to the drag values of the 2-d circular cylinder. These drag values increase with the considered Reynolds numbers (see Fig. 14a). These Reynolds numbers lie in the critical and transcritical regime of the 2-d circular cylinder. The limiting points ($\oplus$, ∇, Λ) of Figure 14a are the drag values of the 2-d circular cylinder. The measured forces seem relatively good to approximate these values.

Figure 14c shows a different Reynolds number characteristic of the side forces in comparison with the results for the higher Mach numbers. One can observe an increase of the side forces with growing Reynolds number. The onset of the side forces is obviously nearly independent of the Reynolds number and occurs also in this case at incidences of about 10°.

The calculated normal forces agree very well with the experimental data up to incidences of about 20° to 35°. At higher angles of attack the normal forces are underestimated by the calculation. A good agreement of the predictions with the measurements was obtained for the slopes of the normal force and pitching moment curves at $\alpha = 0°$. Also the basic characteristic of the side forces is relatively good reproduced if one takes into consideration the complicated flow phenomena. The direction of the side forces and the yawing moments is arbitrary in the experiment. For that reason the sign of the calculated characteristics was adapted to the experiment.

Body-tail and body-wing-tail combinations

All combinations have non-linear force and moment characteristics with respect to the angle of attack. These non-linearities are strongest for the +-positions of the lifting surfaces and the smaller aspect ratio. They are weakest for the body-wing-tail combination in the ×-position (see Fig. 13). Figure 15 shows for this combination the Reynolds number dependence of the normal and side forces. The observed trends reflect in the whole angle of attack range the Reynolds number characteristic of the body as can be seen by a comparison with Figure 14.

The onset of the side forces occurs for the body-tail and body-wing-tail combinations at different angles of attack. In the case of the body-wing-tail combination the onset of the side forces is shifted to higher incidences of 20° or 40°, respectively. The higher angle of attack belongs to the ×-position of the combination.

The trends of all normal force and pitching moment curves show an interesting common feature. This is a distinct decrease of the slopes of the characteristics at incidences of about 10°. This effect is especially evident in the case of the body-tail combination with 4D span. The measurements shown in Figures 9 to 13 clearly demonstrate that this phenomenon depends upon the aspect ratio of the rectangular wing, the roll orientation of the combination (+- or ×-position), the Mach number and the local angle of attack of the lifting surfaces. It was attempted in section V.1 (Calculations) to give an interpretation of this fact. The relating calculations seem to confirm this statement. But it must kept in mind that downwash effects can contribute some similar effects, particularly when a body-wing-tail combination is considered in ×-position.

For all combinations the calculations reproduce the linear and non-linear parts of the normal forces and pitching moments relatively well up to angles of attack of about 10°. At higher incidences the calculated values are overestimated. Some questions arise from Figure 10b, where the degressive pitching moment characteristic at small angle of attack cannot be fully understood.

For the body-tail combinations the onset of the side forces and the following trends are reproduced fairly well.

VI. Conclusions

For engineering purposes measurements of body, body-tail and body-wing-tail combinations were presented and compared with an analytical method which is based on the approach of coefficient synthesis. For the body alone the calculations provide reasonable results up to high angles of attack. The prediction of the characteristics of the body-tail and body-wing-tail combinations turned out to be more difficult at higher angles of attack due to the massive flow separation on the lifting surfaces. It is concluded that an improvement of the prediction method within the scope of a coefficient synthesis must comprise an enlargement of an empirical data base for wings and the development of theoretical flow models of the separated flow over arbitrary shaped wings. The Reynolds number influence for the body is to be taken into account, too. Further experiments are needed in order to clarify the characteristics of the moment curves obtained for the body-tail combination.

VII. References

(1)   K. Hartmann: Experimental Investigation on an Ogive-Nosed Body at High Incidence and Different Reynolds Numbers. Proceedings of the International Conference on Fluid Mechanics; Beijing, China, July 1-4, 1987.

(2)   V. Kanagarajan, K. Hartmann: Force Measurements on a Body-Tail Combination at Different Reynolds Numbers and Roll Angles up to Incidences of 45°. DFVLR IB 222-85 A 38.

(3)   V. Kanagarajan, K. Hartmann: Force Measurements on a Body-Wing-Tail Configuration (KaHa Model) at Mach Numbers of 0.4, 0.6 and 0.8 and Incidences up to 30°. DFVLR IB 222-87 A 25.

(4) V. Kanagarajan, K. Hartmann: Force Measurements on a Body-Wing-Tail Configuration (KaHa Model) at Mach Numbers of 0.4, 0.6 and 0.8 and Incidences from 30° to 65°. DFVLR IB 222-87 A 27.

(5) H. Ludwieg, Th. Hottner: Hochgeschwindigkeitskanal der Aerodynamischen Versuchsanstalt Göttingen. Z. Flugw. 7 (1959), Heft 10.

(6) H. Ludwieg, Th. Hottner: Die Überschall-Meßstrecke (710 mm × 725 mm) des Hochgeschwindigkeitskanals der AVA. Z. Flugw. 11 (1963), Heft 4.

(7) H. Försching, E. Melzer, G. Schewe: Ein neuer Windkanal für gebäudeaerodynamische und -aeroelastische Untersuchungen bei Reynoldszahlen bis 10⁷. Konstruktiver Ingenieurbau Bericht Heft 35/36, 1981, Seiten 127-133.

(8) D. Nikolitsch: Normal Force and Pitching Moment Coefficient of Bodies and Wing-Body Combinations at Very High Angles of Attack. AIAA paper 78-63 (1978), AIAA 16th aerospace sciences meeting, Huntsville, Alabama, Jan. 1978.

(9) D. Nikolitsch: Calculation of Pressure Distributions, Forces and Moments of Cruciform Wing-Body Combination up to High Angles of Attack. AIAA paper 81-0398 (1981), AIAA 19th aerospace sciences meeting, St. Louis, Missouri, Jan. 1981.

(10) D. Nikolitsch, E. Waxweiler: Berechnung der Rollmomentenbeiwerte von Flügel-Rumpf-Kombinationen bei hohen Anstellwinkeln im Unterschall. MBB Bericht TN AE 12-5/81 (1981).

(11) P. Hennig, E. Hartner: Instationäre Beiwerte von Flugkörpern. Teil V: Derivative der Längsstabilität von Flügel-Rumpf-Leitwerk Anordnungen in Unter- und Überschallströmung. MBB Bericht UA-830-84 (1984).

(12) W.C. Pitts, J.N. Nielsen, G.E. Kaattari: Lift and Center of Pressure of Wing-Body-Tail Combination at Subsonic, Transsonic and Supersonic Speeds. NACA Report 1307 (1957).

(13) H. Esch: Normalkraft- und Kippmomentmessung an schlanken Flugkörperflügeln im unteren Transschallbereich bei großen Anstellwinkeln. DFVLR IB 391-82 A 02.

(14) K. Hartmann: Influence of the Reynolds Number on the Normal Forces of Slender Bodies of Revolution. NASA TM-76710, May 1982; and Z. Flugwiss. Weltraumforsch. 2 (1978), Heft 1, S. 22-35 (German original of preceding English title).

(15) K. Hartmann: Pressure and Force Distributions on an Ogive-Nosed Circular Cylinder at High Angles of Attack in an Incompressible Airstream. DFVLR IB 222-83 A 05.

(16) H. Esch: Der Einfluß der Reynoldszahl auf die Normalkraftcharakteristik schlanker zylindrischer Rümpfe. DLR-FB 75-09 (1975).

α	Ma	Re×10 E-6	Type of wind tunnel
-5°÷67°	0.4	0.28	High speed wind tunnel HKG
	0.6	0.39	
	0.8	0.47	
-2°÷70°	< 0.1	0.70	0.6m pressurized low speed wind tunnel HDG
		2.05	
		4.15	
		5.75	

Table 1. Test program
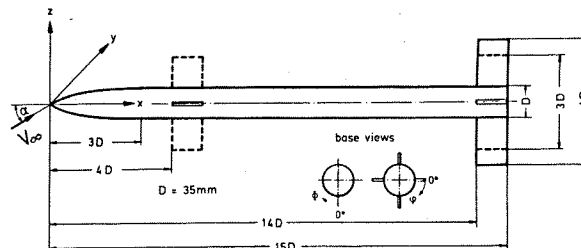
Figure 1. Geometrical details of the various model configurations
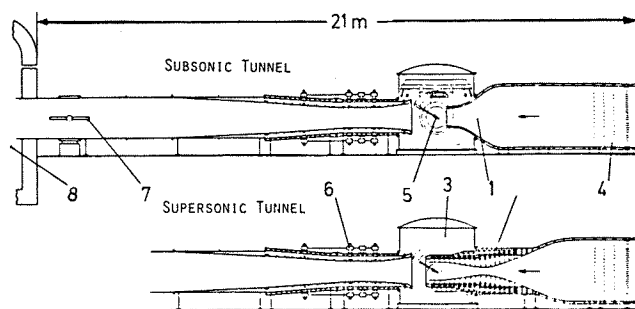
1. Subsonic nozzle (75 cm × 75 cm)
2. Supersonic flexible nozzle (71 cm × 72,5 cm)
3. Vacuum-proof plenum chamber
4. Grids and honeycombs
5. Balance and model
6. Convergent-divergent adjustable diffusor
7. Butterfly valve
8. Vacuum storage vessel

Figure 2. High speed wind tunnel (HKG) of the DFVLR/AVA
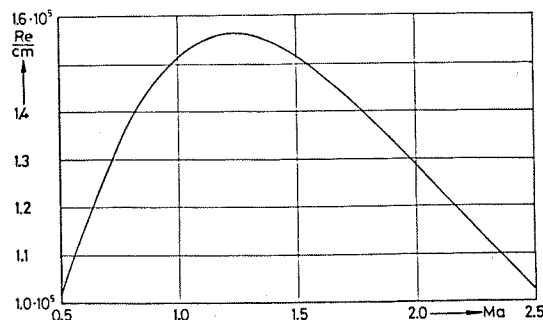
Figure 3. Reynolds number per cm as function of the Mach number for the high speed wind tunnel of the DFVLR/AVA

1875
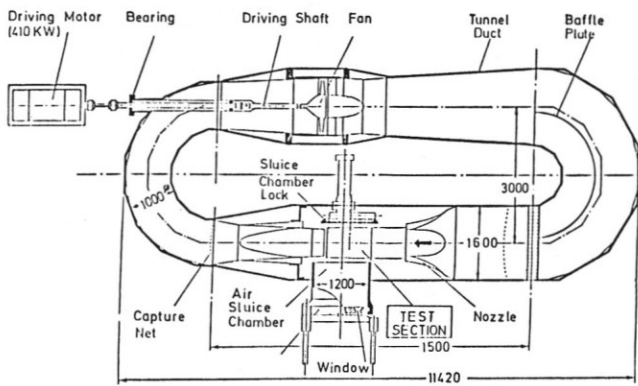
Total volume including sluice chamber = 38.1 m³

Test section details : Interchangeable ; open / close

Size = 0.6m x 0.6m x 1m

Area = 0.36 m²

Figure 4. 0.6m pressurized low speed wind tunnel of the DFVLR/AVA
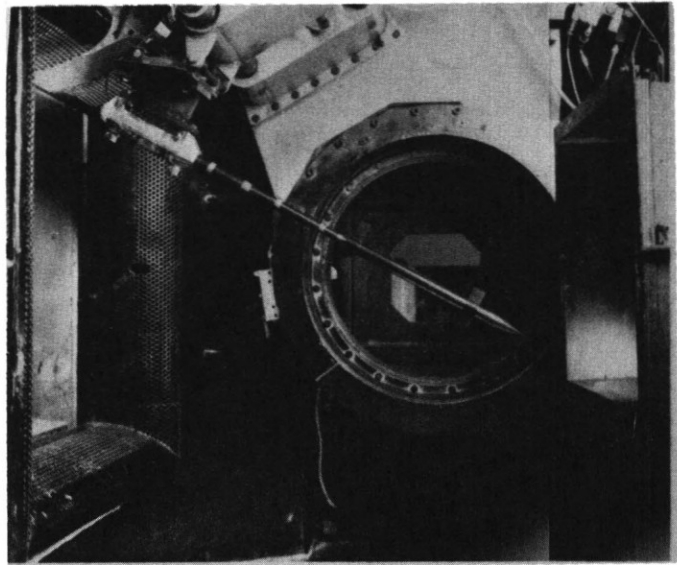
Figure 6. Wind tunnel test setup

q_∞ [da Pa]

$t = 15°C$

$q_\infty = \frac{1}{2} \rho V_\infty^2$

$Re = \frac{V_\infty \cdot l}{\eta(p,T)} \rho$
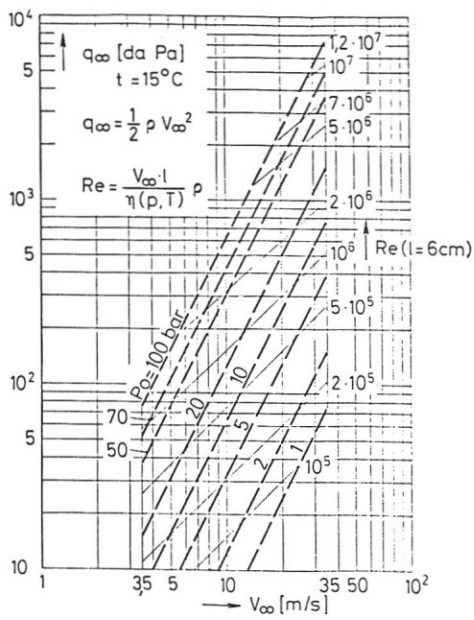
Figure 5. Performance envelope of the 0.6m pressurized low speed wind tunnel of the DFVLR/AVA
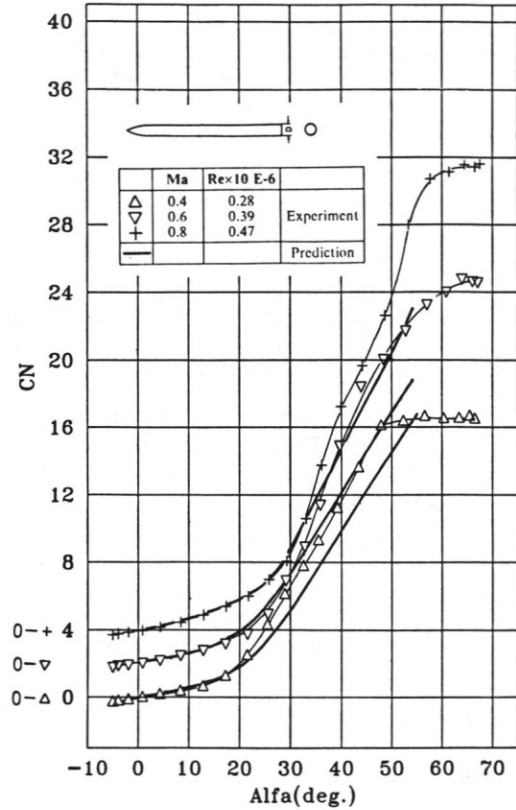
Figure 7a. Variation of normal force coefficient with angle of attack and comparison with theory. Body roll angle $\phi = 60°$
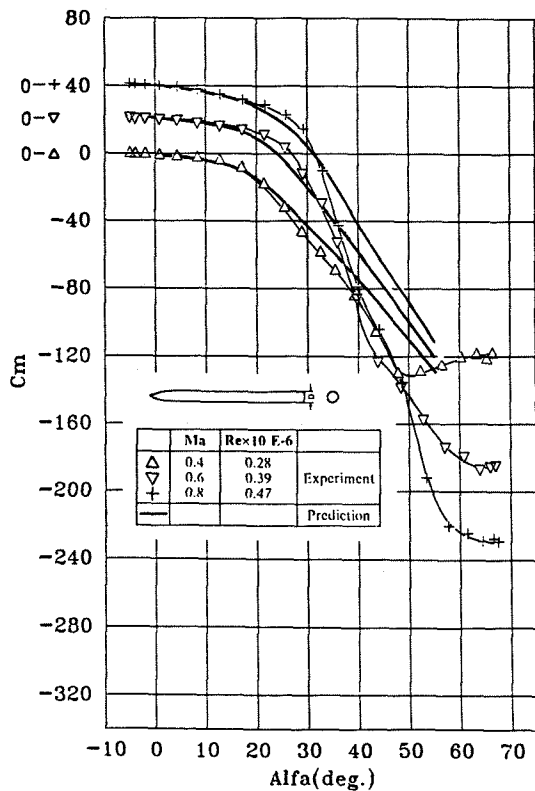
Figure **7b**. Variation of pitching moment coefficient with angle of attack and comparison with theory. Body roll angle Φ = 60°
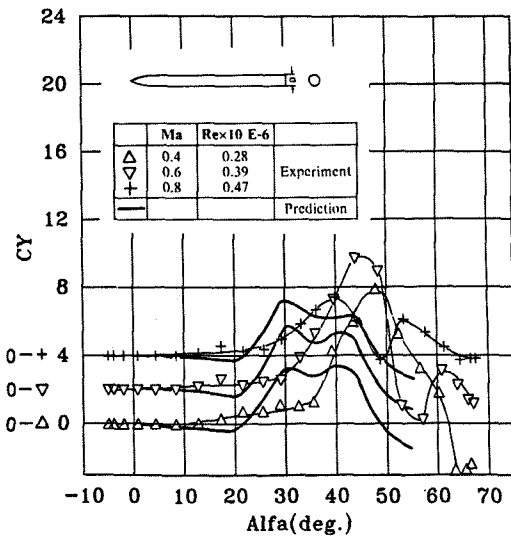
Figure **7c**. Variation of side force coefficient with angle of attack and comparison with theory. Body roll angle Φ = 60°
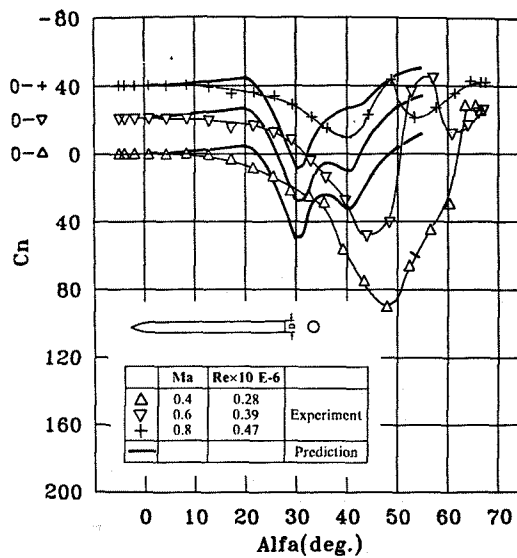
Figure **7d**. Variation of yawing moment coefficient with angle of attack and comparison with theory. Body roll angle Φ = 60°
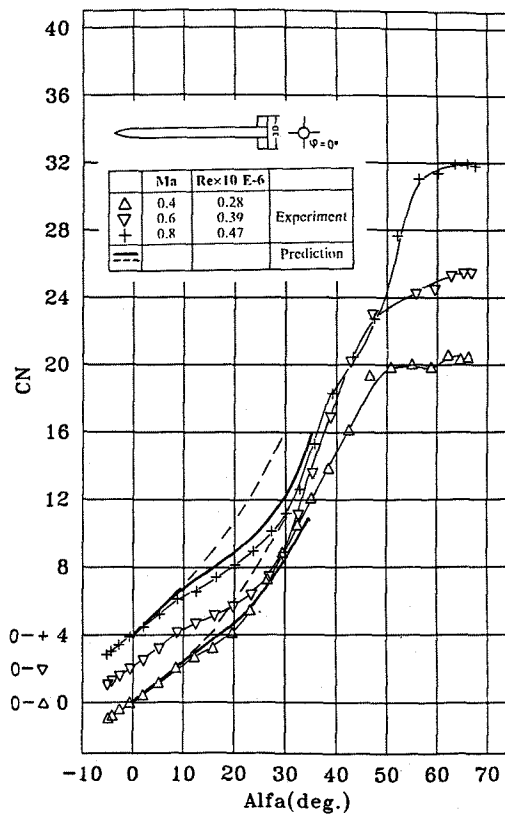
Figure 8a. Variation of normal force coefficient with angle of attack and comparison with theory. All lifting surfaces in + position

——————— Calculation with correction beyond $\alpha_{crit.}$ (Fig. 16)

— — — — Calculation without correction beyond $\alpha_{crit.}$ (Fig. 16)

1877
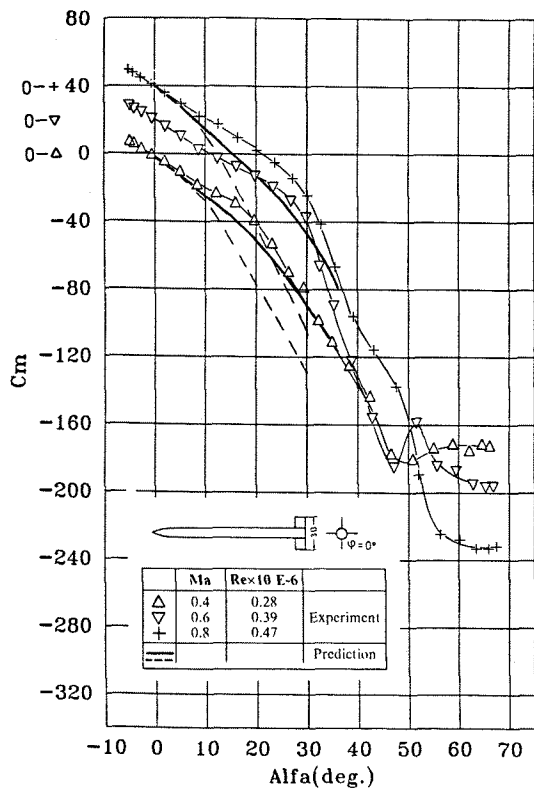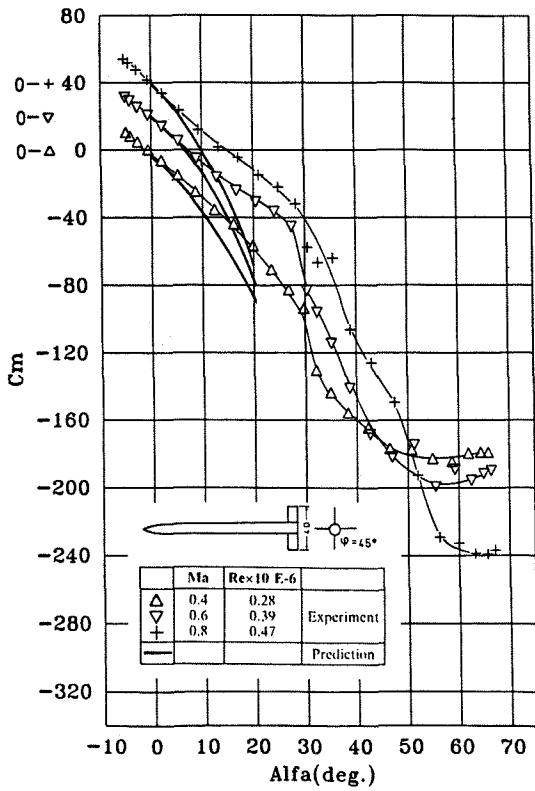
Figure 8b. Variation of pitching moment coefficient with angle of attack and comparison with theory. All lifting surfaces in + position

———— Calculation with correction beyond $\alpha_{crit.}$ (Fig. 16)

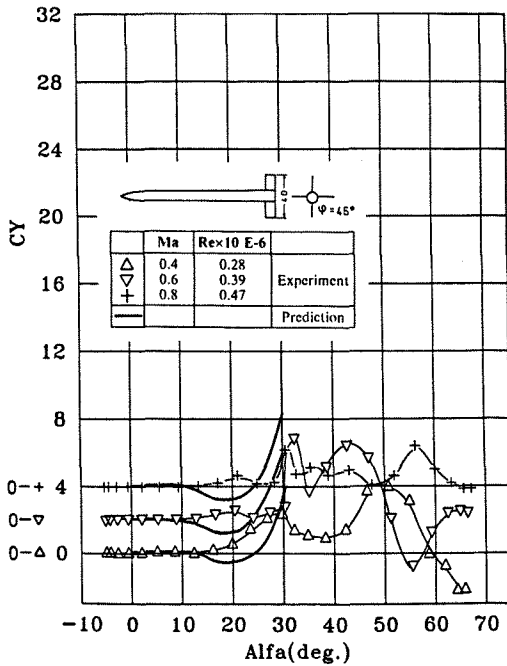— — — Calculation without correction beyond $\alpha_{crit.}$ (Fig. 16)
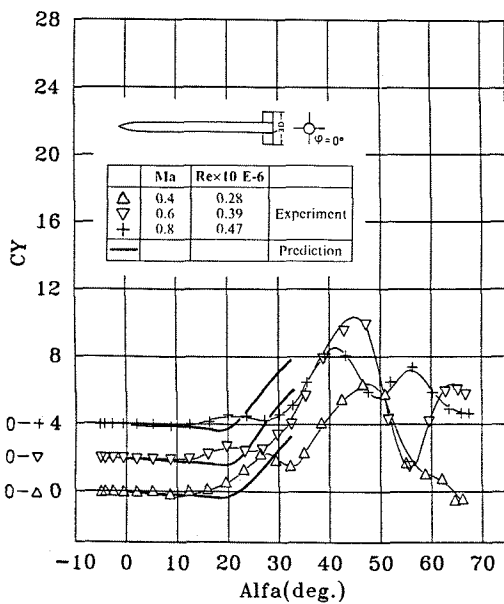
Figure 8c. Variation of side force coefficient with angle of attack and comparison with theory. All lifting surfaces in + position
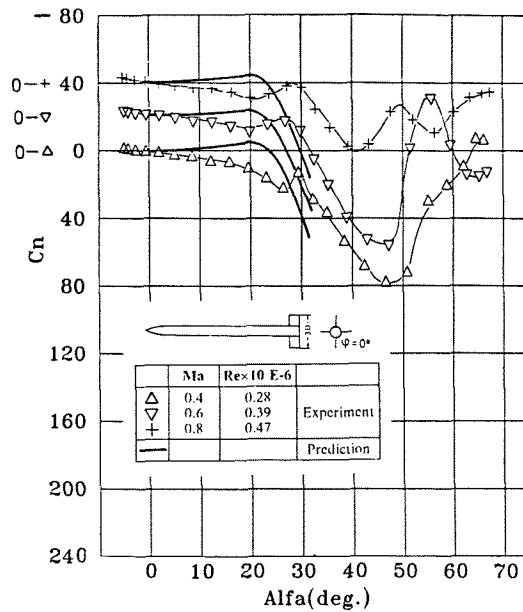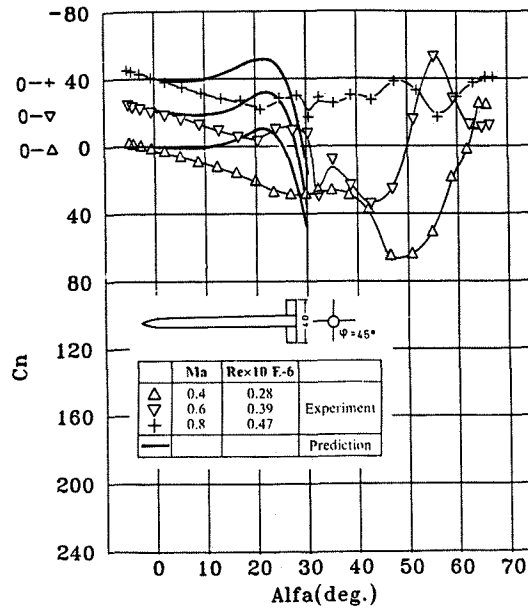
Figure 8d. Variation of yawing moment coefficient with angle of attack and comparison with theory. All lifting surfaces in + position
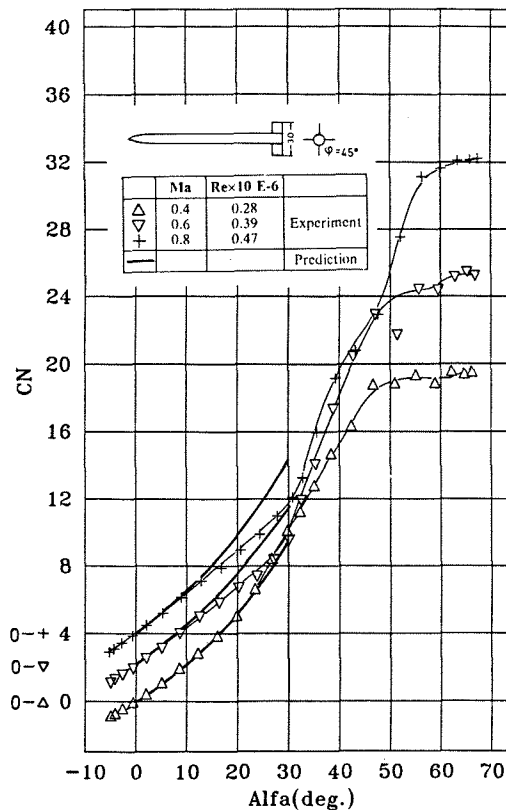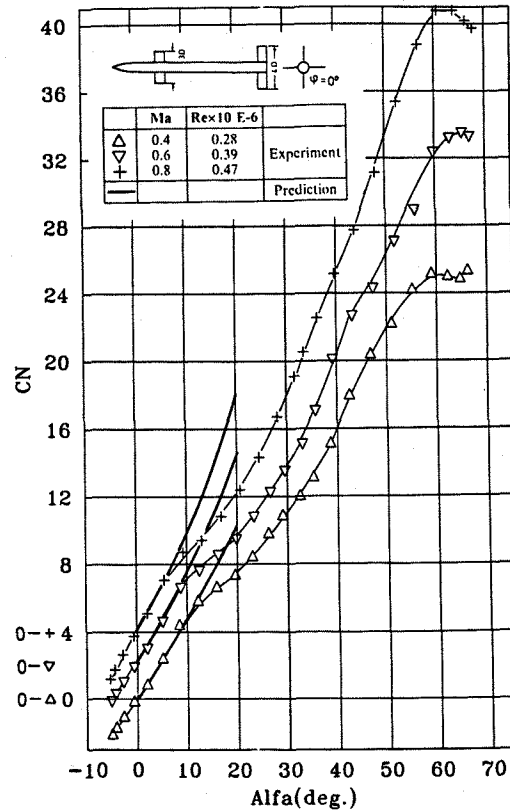
Figure 9a. Variation of normal force coefficient with angle of attack and comparison with theory. All lifting surfaces in x position
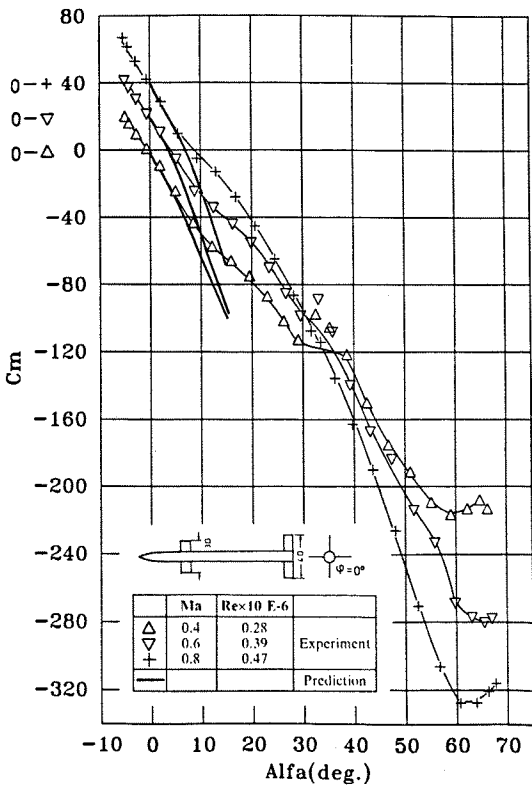
	Ma	Re×10 E-6	
△	0.4	0.28	Experiment
▽	0.6	0.39	
+	0.8	0.47	
—			Prediction

1878
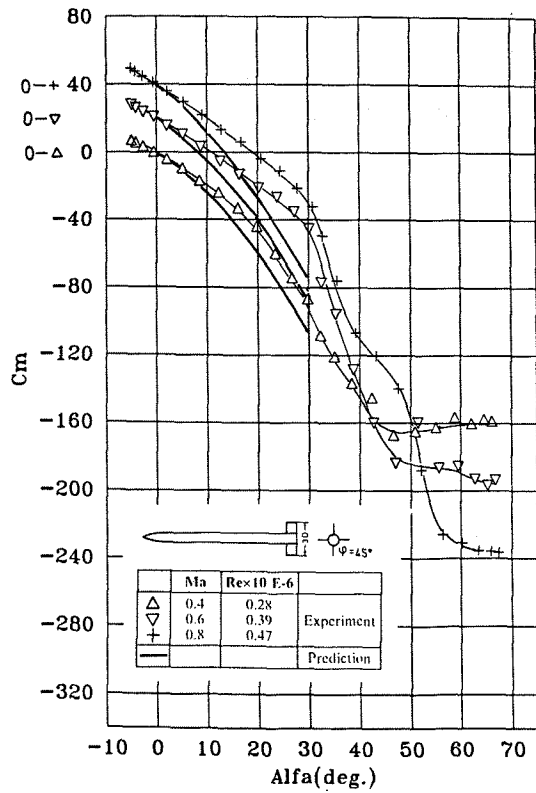
Figure 9b. Variation of pitching moment coefficient with angle of attack and comparison with theory. All lifting surfaces in x position
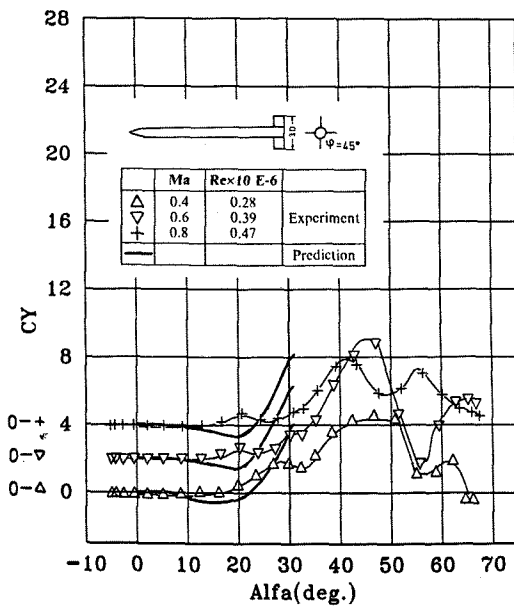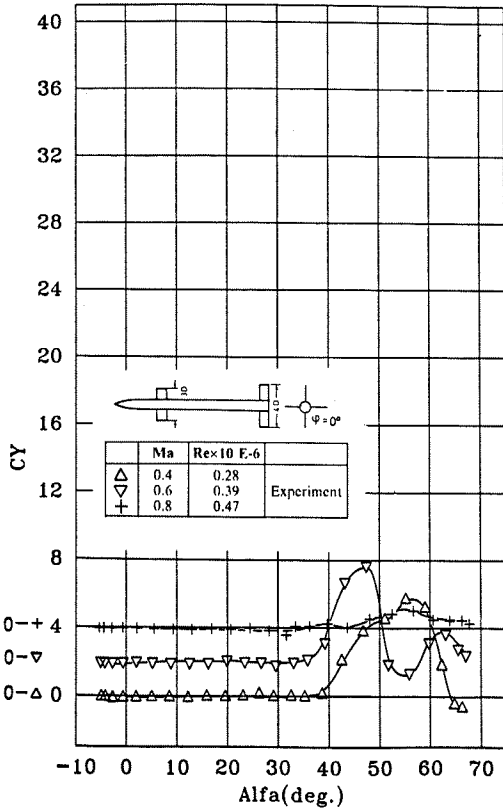

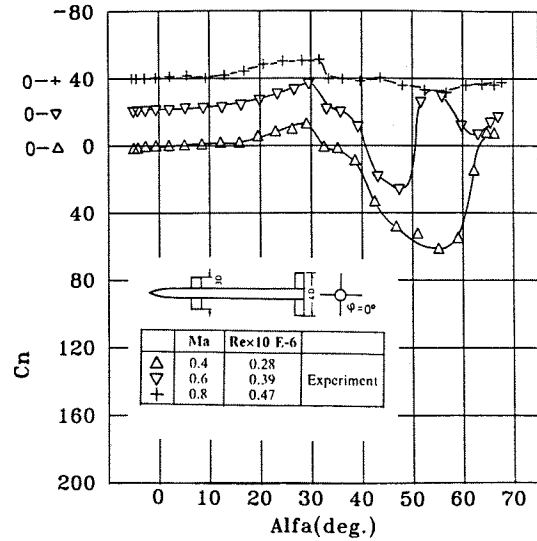**Figure 9c.** Variation of side force coefficient with angle of attack and comparison with theory. All lifting surfaces in x position
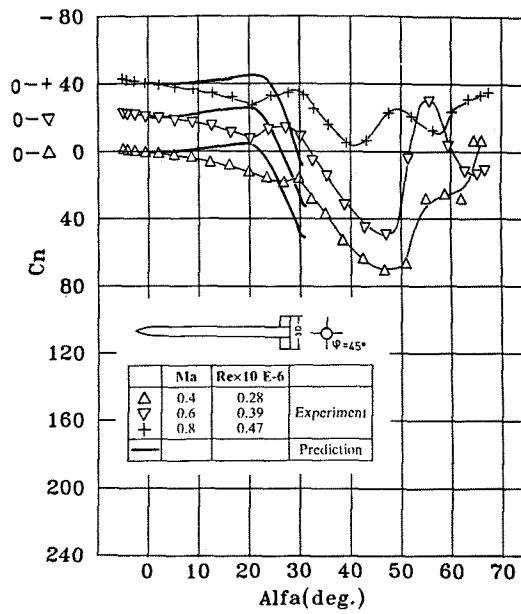
Figure 9d. Variation of yawing moment coefficient with angle of attack and comparison with theory. All lifting surfaces in x position
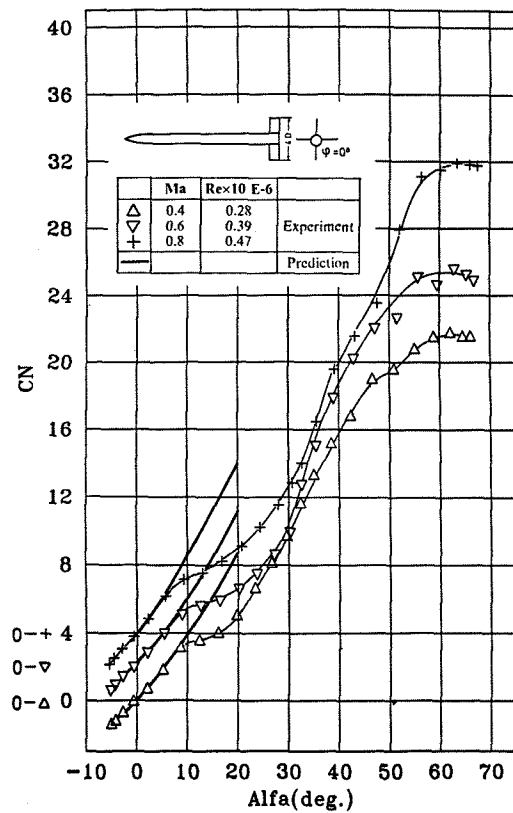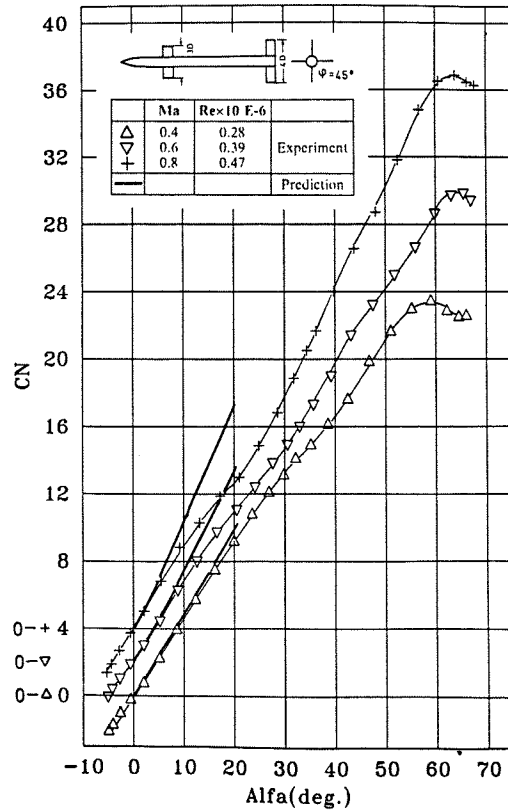

Figure 10a. Variation of normal force coefficient with angle of attack and comparison with theory. All lifting surfaces in + position
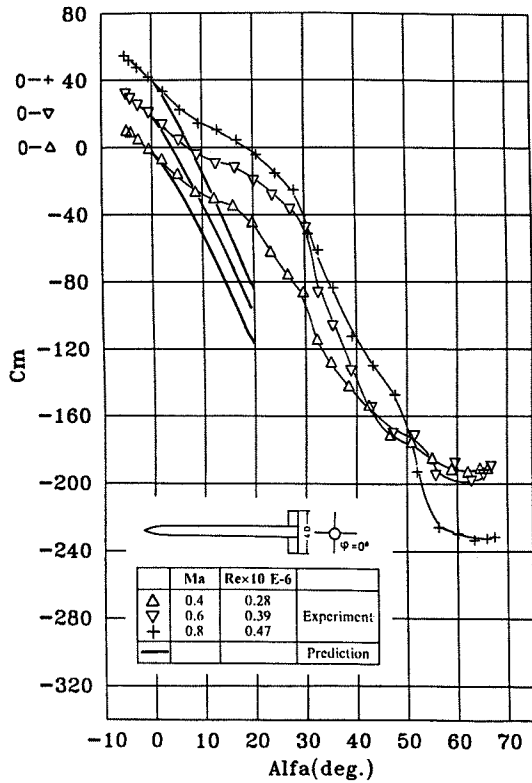
Figure 10b. Variation of pitching moment coefficient with angle of attack and comparison with theory. All lifting surfaces in + position
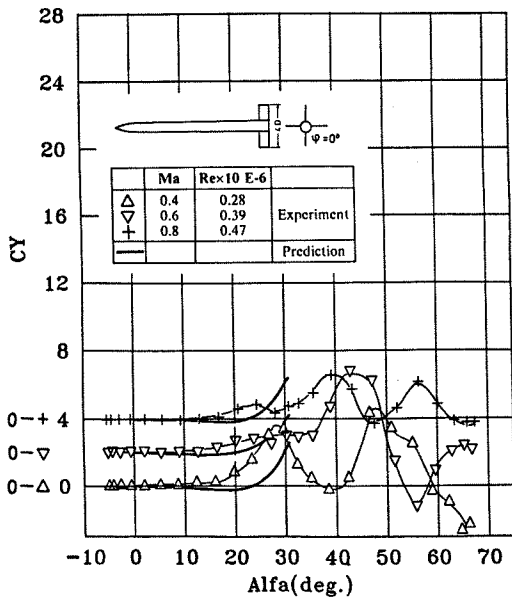
Figure 10c. Variation of side force coefficient with angle of attack and comparison with theory. All lifting surfaces in + position
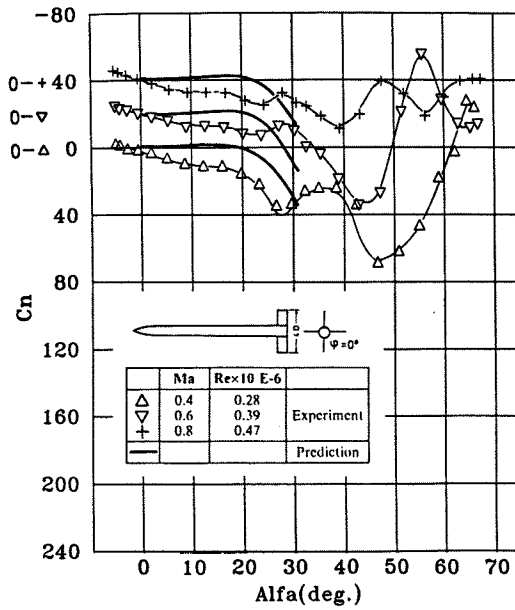
Figure 10d. Variation of yawing moment coefficient with angle of attack and comparison with theory. All lifting surfaces in + position
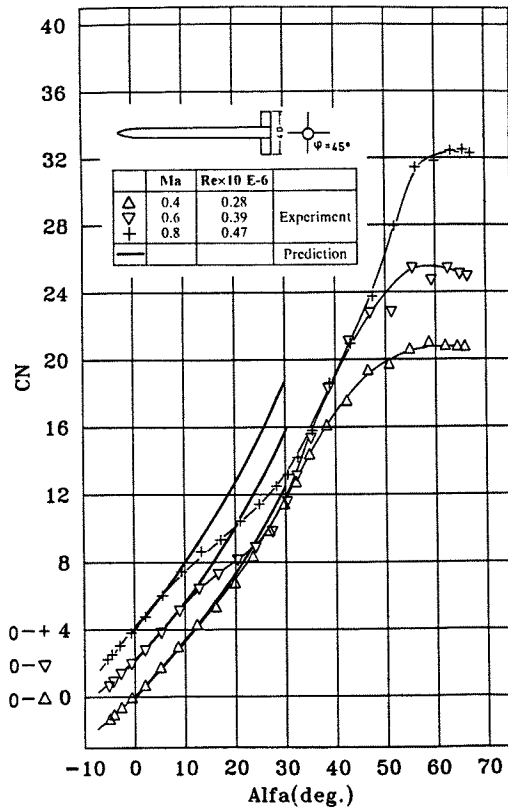
Figure 11a. Variation of normal force coefficient with angle of attack and comparison with theory. All lifting surfaces in x position
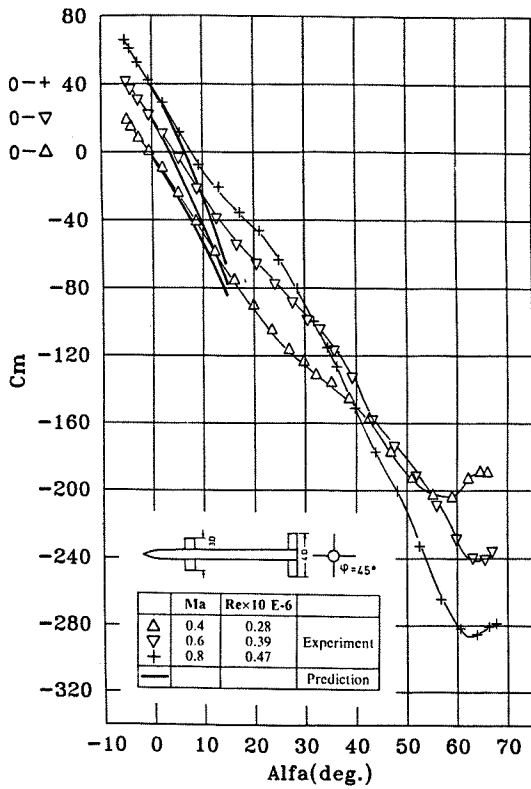
1880

Figure 11b. Variation of pitching moment coefficient with angle of attack and comparison with theory. All lifting surfaces in x position
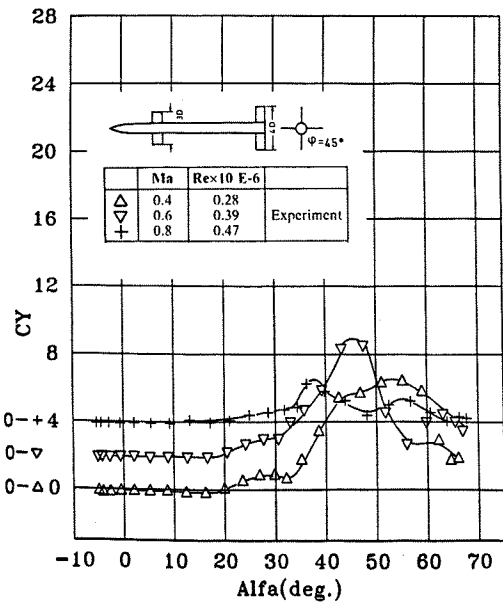
Figure 11c. Variation of side force coefficient with angle of attack and comparison with theory. All lifting surfaces in x position

Figure 11d. Variation of yawing moment coefficient with angle of attack and comparison with theory. All lifting surfaces in x position

Figure 12a. Variation of normal force coefficient with angle of attack and comparison with theory. All lifting surfaces in + position

Figure 12b. Variation of pitching moment coefficient with angle of attack and comparison with theory. All lifting surfaces in + position

Figure 12c. Variation of side force coefficient with angle of attack. All lifting surfaces in + position
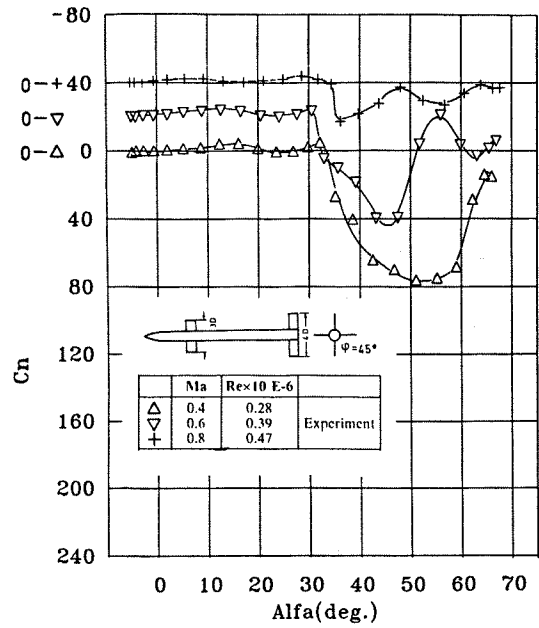

Figure 12d. Variation of yawing moment coefficient with angle of attack. All lifting surfaces in + position


Figure 13a. Variation of normal force coefficient with angle of attack and comparison with theory. All lifting surfaces in x position

1882

Figure 13b. Variation of pitching moment coefficient with angle of attack and comparison with theory. All lifting surfaces in x position

Figure 13c. Variation of side force coefficient with angle of attack. All lifting surfaces in x position

Figure 13d. Variation of yawing moment coefficient with angle of attack. All lifting surfaces in x position
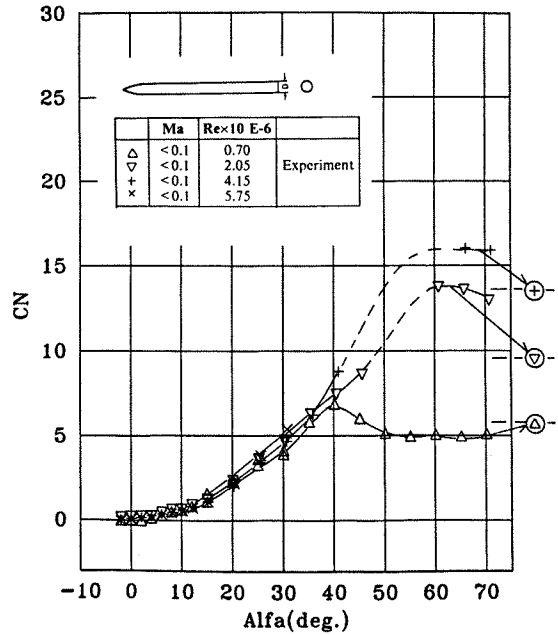
Figure 14a. Reynolds number influence on the normal force characteristics at Ma < 0.1, body alone
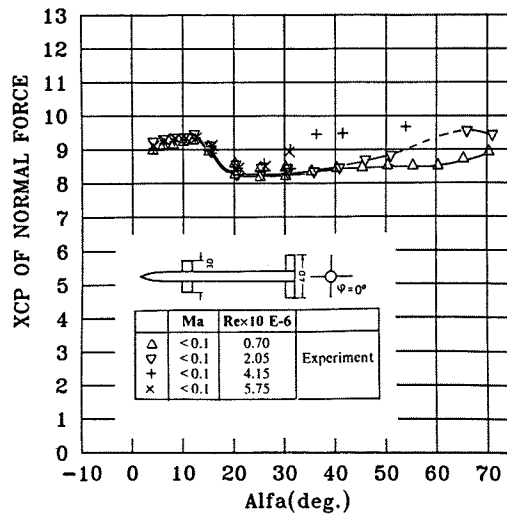
1883
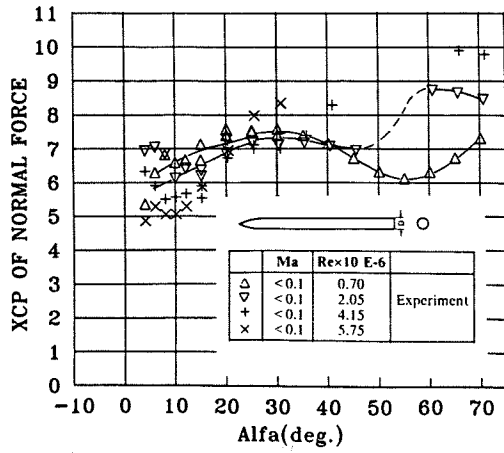
Figure 14b. Reynolds number influence on the center of pressure at Ma < 0.1, body alone

Figure 14c. Reynolds number influence on the side force characteristics at Ma < 0.1, body alone

Figure 15a. Reynolds number influence on the normal force characteristics at Ma < 0.1, body-wing-tail configuration

Figure 15b. Reynolds number influence on the center of pressure at Ma < 0.1, body-wing-tail configuration

1884
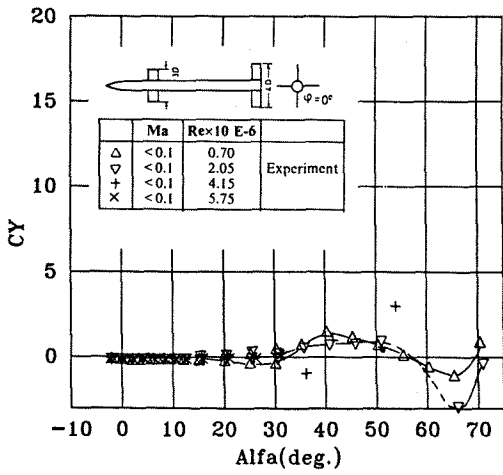
Figure 15c. Reynolds number influence on the
side force characteristics at
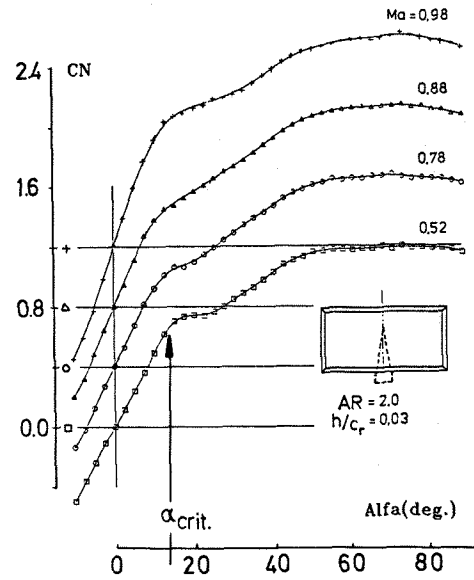Ma < 0.1, body-wing-tail configuration

Figure 17a. Normal force characterisitcs of a
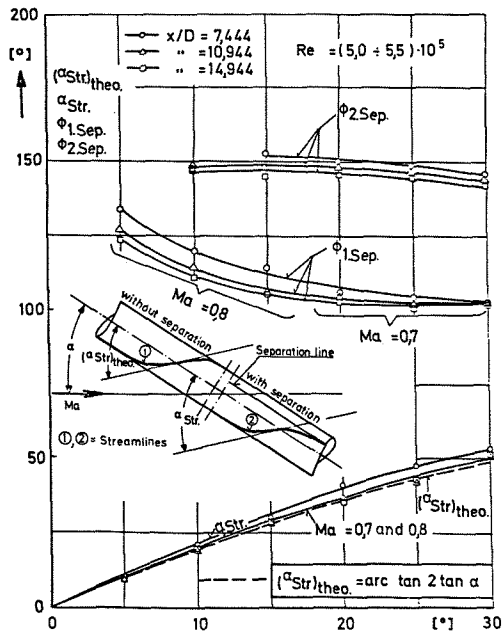rectangular wing with sharp edges

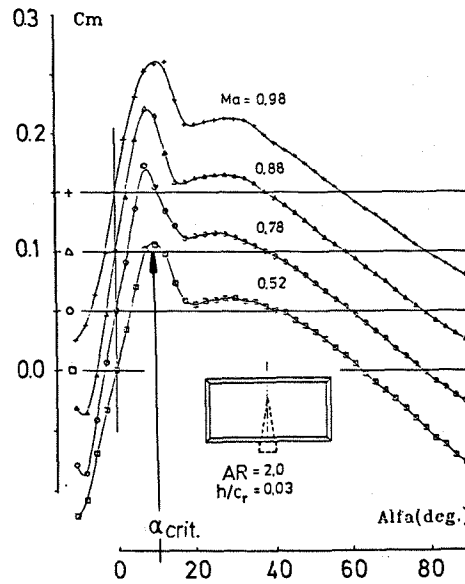Figure 16. Separation lines and streamlines on
the body alone

Figure 17b. Pitching moment characteristics of
a rectangular wing with sharp edges.
Moment reference point = center of
wing area

1885